Applied Energy 186 (2017) 359–375

Contents lists available at ScienceDirect

Applied Energy

journal homepage: www.elsevier.com/locate/apenergy

A two-phase single-reciprocating-piston heat conversion engine: Non-linear dynamic modelling

Christoph J.W. Kirmse, Oyeniyi A. Oyewunmi, Aly I. Taleb, Andrew J. Haslam, Christos N. Markides *

Clean Energy Processes (CEP) Laboratory, Department of Chemical Engineering, Imperial College London, South Kensington Campus, London SW7 2AZ, UK

HIGHLIGHTS

- We developed a non-linear dynamic model for the thermofluidic oscillator Up-THERM.
- The gas spring model and temperature profile were validated experimentally.
- The experiments show good agreement with the model predictions.
- A parametric study with the validated model was carried out.
- Depending on the design of the engine, high exergy efficiencies can be achieved.

ARTICLE INFO

Article history:
Received 12 October 2015
Received in revised form 20 May 2016
Accepted 23 May 2016
Available online 29 June 2016

Keywords:
CHP prime mover
Electrical analogy
Energy conversion
Heat engine
Non-linear
Reciprocating piston
Thermofluidic oscillator
Two phase
Unsteady

ABSTRACT

A non-linear dynamic framework is presented for the modelling of a novel two-phase heat engine termed 'Up-THERM', which features a single solid moving-part (piston). When applied across the device, a constant temperature difference between an external (low- to medium-grade) heat source and an external heat sink is converted into sustained and persistent oscillations of pressure and volumetric fluid displacement. These oscillations are transformed in a load arrangement into a unidirectional flow from which power is extracted by a hydraulic motor. The Up-THERM engine is modelled using a system of first-order differential equations that describe the dominant thermal/fluid processes in each component of the device. For certain components where the deviations from a linear approximation are non-negligible (gas spring in the displacer cylinder, check valves and piston valve, and heat exchangers), a non-linear description is employed. A comparison between the linear and non-linear descriptions of the gas spring at the top of the displacer cylinder reveals that the non-linear description results in more realistic predictions of the oscillation frequency compared to experimental data from a similar device. Furthermore, the shape of the temperature profile over the heat-exchanger surfaces is modelled as following a hyperbolic tangent function, based on findings from an experimental investigation. Following the validation of these important device components, a parametric study is performed on the Up-THERM engine model with the aforementioned non-linear component descriptions, aimed at investigating the effects of important geometric parameters and of the heat-source temperature on key performance indicators, namely the oscillation frequency, power output and exergy efficiency of the engine. The results indicate that the geometric design of the displacer cylinder, including the height of the gas spring at the top of the cylinder, and the heat-source temperature have the most significant influence on the performance of the engine. A maximum exergy efficiency of 2.8% and a maximum power output of 175 W are observed at the proposed operating temperature of 450 °C for a nominal Up-THERM design (based on the physical dimensions of a device prototype and water as the working fluid; the role of the working fluid is explored in follow-up paper Ref. [1]) but with shorter displacer cylinder gas-spring lengths relative to a nominal design. The results and insight can assist the further development of this technology, in particular as a prime mover in combined heat and power applications.

* Corresponding author.
E-mail address: c.markides@imperial.ac.uk (C.N. Markides).

http://dx.doi.org/10.1016/j.apenergy.2016.05.140
0306-2619/

Nomenclature

A	cross-sectional area (m^2)
C	capacitance ($m^4\ s^2/kg$)
c	geometrical constant (–)
d	diameter (m)
ΔE	voltage difference (V)
F	force (N)
f	frequency (Hz)
g	gravitational acceleration (m/s^2)
H	Heaviside step function
h	height (m)
h	heat transfer coefficient ($W/m^2\ K$)
I	rotational inertia ($kg\ m^2$)
I	electrical current (A)
K	non-dimensional expression for α (–)
k	spring constant (N/m)
L	inductance (kg/m^4)
l	length (m)
m	mass (kg)
P	pressure (Pa)
P_{hm}	power output (W)
$\dot{Q}$	heat flow-rate (W)
R	resistance ($kg/m^4\ s$)
r	radius (m)
$\dot{S}$	rate of entropy generation (W/K)
T_{hm}	torque hydraulic motor (N m)
T	temperature (K)
t	time (s)
U	flow rate (m^3/s)
V	volume (m^3)
y	spatial coordinate (–)

Greek letters

α	temperature amplitude (K)
β	parameter that depends on the spatial gradient of the heat-exchanger wall temperature at equilibrium (1/m)
γ	heat-capacity ratio (–)
δ	gap between piston and slide bearing (m)
ϵ	gap between shaft and motor (m)
η	efficiency (–)
Λ	non-dimensional expression for β (–)
μ	dynamic viscosity (m^2/s)
ρ	density (kg/m^3)
ω	angular velocity (rad/s)

Subscripts

'0'	equilibrium
'a'	accumulator
'ar'	argon
'b, l'	slide bearing liquid
'b, p'	slide bearing piston
'c'	connection tube
'cold'	cold heat exchanger
'cv'	check valve
'd'	displacer cylinder
'ex'	exergy
'fg'	phase change
'fric'	friction
'g'	generator
'gen'	gas volume
'gs'	gas spring
'hm'	hydraulic motor
'hot'	hot heat exchanger
'hx'	heat exchanger
'l'	liquid volume
'l, d'	liquid height in the displacer cylinder
'load'	load
'lub'	lubricant
'max'	maximum
'min'	minimum
'ms'	mechanical spring
'nl'	non-linear
'p'	piston
'p*'	pressure
'pv'	piston valve
'q'	heat flux
'sat'	saturation
'sh'	shaft
't'	pipe in load
'th'	thermal domain
'v'	vapour volume
'w'	wall
'wf'	working fluid

Superscript

'*'	scaling parameter

1. Introduction

Continuing increases in global energy demand and usage in conjunction with a heavy reliance on the combustion of fossil fuels have led to the increased consumption of finite fossil-fuel resources and of related gaseous emissions into the atmosphere [2]. The need to halt and possibly reverse this trend has been motivating research into the exploitation of alternative sources of energy, such as solar or geothermal heat. The temperature level of these energy sources is typically lower than in conventional power plants (from <100 °C up to ~350 °C for geothermal [3], and up to ~550 °C for parabolic-trough or tower concentrated solar [4]). A further source of low- to medium-grade energy is waste heat, for example from the transport, residential, commercial and public sectors, or from industrial processes [5]. If one could convert this waste heat into useful work, such as electricity, shaft/mechanical or hydraulic work depending on the need, the overall efficiencies of a vast array of processes and systems could be significantly improved [6].

Due to their lower temperatures, these heat sources cannot be efficiently utilised in conventional cycles, since the resulting thermal efficiency is inherently low. One particular class of engine that is suitable for the affordable utilisation of low-grade heat is the thermofluidic oscillator. The simple construction (few moving parts or dynamic seals) of thermofluidic oscillators allow these devices to have low capital and maintenance costs, in addition to long lifetimes. Single-phase thermofluidic oscillators include Sondhauss tubes [7,8], standing-wave thermoacoustic engines [9–12], and liquid-piston Stirling engines [13]. The 'Non-Inertive-Feedback Thermofluidic Engine' (NIFTE) is an example of a two-phase thermofluidic oscillator [14–16], which can operate over temperature differences as low as 30 °C.

In the NIFTE, a steady external temperature difference generates and sustains regular thermodynamic oscillations of temperature and pressure that drive fluid flows in the engine from which power can be extracted. Models of NIFTE have been developed and validated against experimental data. It was found that the model predictions were in close agreement with the experimental

measurements of oscillation frequency f_0, temperature gain k and exergy efficiency η_{ex} [17,18]. The NIFTE modelling approach is an excellent starting point for the study of similar two-phase unsteady/oscillatory heat engine concepts.

In the present paper we investigate theoretically a new two-phase thermofluidic oscillator concept termed Up-THERM, proposed and owned by the company Encontech B.V. (www.encontech.nl) [19]. The Up-THERM heat engine is capable of utilising low- to medium-grade heat and of converting this into mechanical work. This technology is being envisioned as an affordable prime-mover in combined heat and power (CHP), or cogeneration, applications. Here, we develop a dynamic modelling framework for the prediction of the operation and performance of this device that is based on the modelling approach taken for the NIFTE; noteworthy non-linear effects are taken explicitly into account. The focus of our work is an examination of the role of the physical dimensions/geometry of the engine on its performance.

In an attempt to validate our modelling approach, we also proceed to measure experimentally for the first time the temperature profile that the working fluid is exposed to as it flows over the heat exchanger surfaces of this two-phase thermofluidic oscillator. An experimental apparatus is developed which is capable of measuring the temperature profile in the heat exchangers under oscillatory operating conditions, whilst the time-varying pressure in the displacement cylinder and the displacement of the piston are recorded.

In the remainder of this paper we firstly introduce the Up-THERM two-phase thermofluidic oscillator heat-engine concept and its operation as proposed by Glushenkov et al. [19], as well as the specific design of a prototype by Encontech B.V. We then develop the Up-THERM engine dynamic modelling framework. Emphasis is given to the derivation of the models of key non-linear components. The oscillation frequency of the Up-THERM model is validated against experimental data from a similar engine, and the model is adjusted by considering the differences between these two devices. This is followed by a presentation of the experimental apparatus that was designed to study the temperature profile on the Up-THERM's heat-exchanger surfaces. Using the validated Up-THERM model we define a nominal (early-stage) design with the physical dimensions proposed by Glushenkov et al. [19]. Proceeding further, we examine the effects on the engine's performance of variations to important physical dimensions and the external heat-source temperature. From the results we attempt to identify the key engine parameters that influence the frequency, power output, and exergy efficiency of the device. This provides an invaluable insight into the characteristics of the engine, which can be harnessed for the development of improved Up-THERM prototype designs.

2. Methods

2.1. Engine configuration and operation

A schematic of the Up-THERM heat engine is shown in Fig. 1. The engine incorporates hot and cold heat exchangers, which are located at the top of the displacer cylinder. Also inside the displacer cylinder are a solid piston and two mechanical springs, an 'upper' one attached to the lower end of the slide bearing and a 'lower' one attached to the bottom of the displacer cylinder. The piston, together with the inside wall of the displacer cylinder, form the 'piston-valve' arrangement. The displacer cylinder, via the connection tube, is connected to two pipes, each of which contains a check valve and a hydraulic accumulator. The two pipes connect to either side of a hydraulic motor. This arrangement converts the oscillating fluid flow in the connection tube to a unidirectional

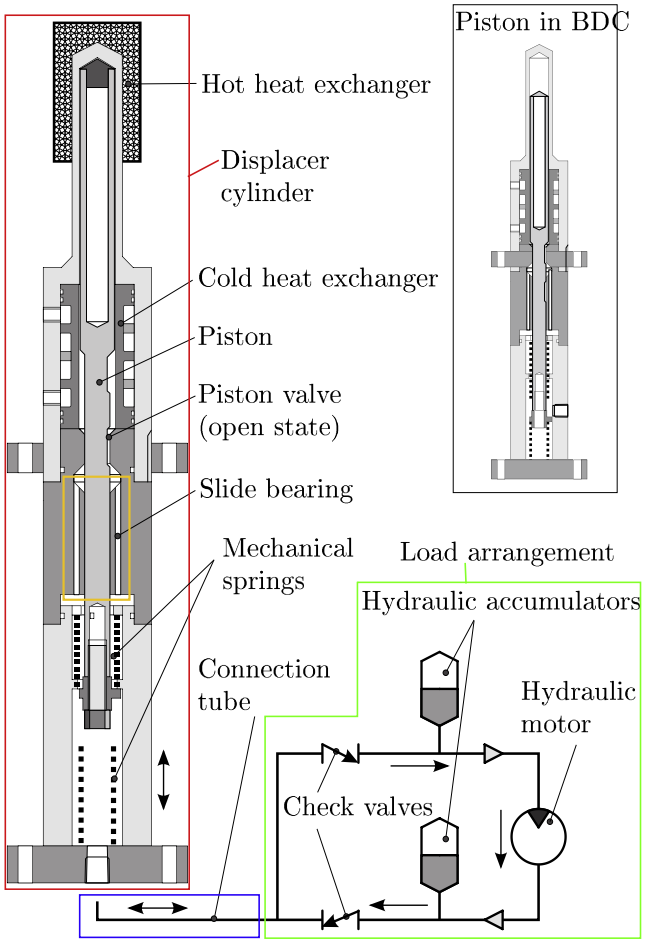

Fig. 1. Schematic of the Up-THERM heat engine with hot and cold heat exchangers, piston, piston valve, upper and lower mechanical springs and hydraulic motor with piston at TDC and BDC (inset).

flow through the hydraulic motor, with damped amplitudes of pressure and volumetric displacement. The space above the piston is filled with working fluid in both vapour (at the very top of the displacer cylinder) and liquid phases. The rest of the engine is filled with liquid working fluid.

It is assumed that at the beginning of the cycle the piston is at the top dead centre (TDC), as depicted in Fig. 1. The piston valve is open and the upper mechanical spring is fully compressed, whilst the lower one is fully relaxed. The vapour-liquid interface is in contact with the hot heat-exchanger (HHX) surface at the upper section of the displacer cylinder and liquid working fluid evaporates, increasing the pressure in the gas-spring space above the piston. This pressure force, together with the extension force from the upper mechanical spring, cause the piston and vapour–liquid interface to move downwards, and the piston valve to close at some point during this motion. From this point in time, fluid is prevented from flowing through the piston valve, and a pressure difference builds up between the compartments above and below the valve. Eventually, as the piston moves even further down, the piston valve re-opens, and the pressures in the upper and lower compartments equalise rapidly as liquid working fluid flows from the upper into the lower compartment. The inertia of the piston and liquid allow the vapour–liquid interface and the piston to overshoot their respective equilibrium positions at the mid-point between the hot and cold heat exchangers. The vapour–liquid interface is now in contact with the surface of the cold heat exchanger (CHX), causing vapour to condense. The upper mechan-

ical spring is now fully relaxed and detaches from the piston whilst the lower one is compressed. The condensing of the vapour and compression of the lower mechanical spring apply restoring forces onto the piston and liquid, such that at the bottom dead centre (BDC) the movements of the piston and vapour–liquid interface reverse. The piston valve closes again which leads to a pressure difference between the upper and lower compartments, causing the piston to move upwards, whilst working fluid is prevented from flowing from the lower to the upper chamber. After the piston valve has opened again, the pressures are equalised rapidly. As before, the piston and vapour–liquid interface overshoot their equilibrium position and the vapour–liquid interface contacts the HHX surface. The upper mechanical spring is compressed until the piston and vapour–liquid interface reach the TDC and one full cycle is complete.

During the cycle, liquid flows in a zero-mean oscillatory manner from the displacer cylinder through the connection tube to the circuit that is connected to the hydraulic motor (see Fig. 1). The check valves in the load-arrangement section of the circuit provide a unidirectional liquid flow through the hydraulic motor where power can be extracted from the cycle. The role of the two hydraulic accumulators is to dampen the pressure and flow oscillations, thereby improving the performance of the hydraulic motor.

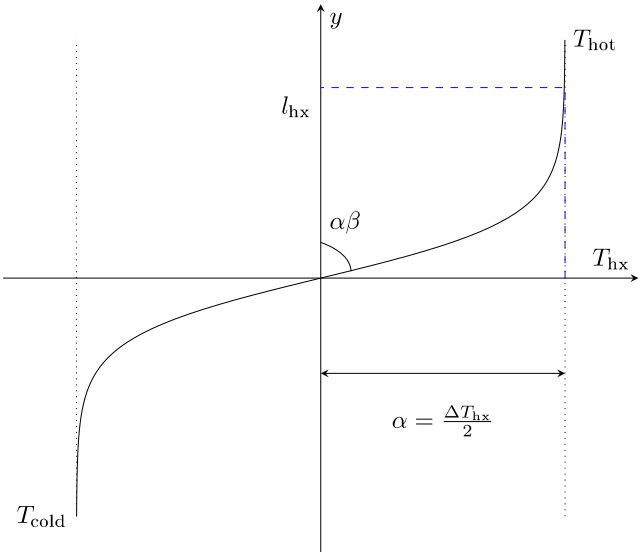

Fig. 2. Non-linear temperature profile over the heat-exchanger surfaces in contact with the working fluid, exhibiting a temperature saturation at $\Delta T_{hx}/2$ on either side of the equilibrium (mean) temperature.

2.2. Model development

The development of the Up-THERM model follows earlier approaches by Ceperley [11], Huang and Chuang [20], Backhaus and Swift [12], and Smith and Markides (who considered the NIFTE) [14–16,21]. Similar to Solanki et al. [22], the effects of liquid inertia are included in the present model. In the model, the engine is separated into thermal and fluid domains. Each domain comprises spatially lumped first-order linearised sub-models where the dominant thermal or fluid-dynamic process in each component is described by an ordinary differential equation. In this work, the piston valve and gas/vapour spring in the displacer cylinder, the two check valves in the load arrangement, and the temperature profile along the vertical height of the heat exchanger walls are modelled non-linearly, whilst all other components are described linearly. These components have been identified as ones in which non-linear behaviour is either intrinsic and therefore unavoidable (e.g. the piston valve and check valves) or necessary in order to capture the correct global behaviour of the Up-THERM device (as observed by a prototype device and related experimental data). This was achieved by testing a number of different Up-THERM models with different non-linearities (plus linearised alternatives) before deciding which ones were necessary to include in the final model presented in the paper. The purpose of Section 3 is to demonstrate how and to what extent the non-linear models of the gas/vapour spring and temperature profile were validated. Analogies are drawn such that the differential equations governing the dynamic processes in each component are represented by passive electrical components (resistors, inductors and capacitors). The individual electrical components are interconnected in the same way as in the physical device (Fig. 1) to form the electrical circuit network shown in Fig. 3.

2.2.1. Thermal domain

The thermal domain comprises the hot and cold heat exchangers and describes the time-varying two-phase heat-transfer process between these components and the working fluid. In the thermal domain heat is converted into fluid flow and pressure, which act as the driving forces for the engine.

A non-linear temperature profile (NTP) along the heat-exchanger walls is used in this work, similar to the NTP model of Markides et al. [18], which allows the temperature to saturate at long lengths from the equilibrium position (half-way between the two heat exchangers). In Fig. 2 the temperature profile along the heat exchanger walls is shown, according to which the profile is described by:

$$T_{hx}(y) = \alpha \tanh(\beta y), \tag{1}$$

where α is the amplitude of the temperature along the heat exchanger walls, or half of the temperature difference between the heat source and sink that set the temperatures along hot and cold heat exchangers ($\alpha = (T_{hot} - T_{cold})/2$). The slope at the origin is equal to the product $\alpha\beta$. The value for β is modelled as scaling with the inverse of the length l_{hx} of one of the heat exchangers ($\beta \sim 1/l_{hx}$), as it is assumed that the temperature profile saturates at the maximum length of the heat exchanger. This temperature profile is later verified in Section 3.4.

In this model, it is assumed that the temperature profile is externally imposed and that it is time invariant. The convective heat transfer due to phase-change at the vapour–liquid interface is assumed to be much greater than the convective heat transfer which takes place at areas away from that interface. From Fig. 2 one can see that T_{hx} varies with the position y of the vapour–liquid interface relative to the equilibrium position. This distance in turn varies with time, so that $T_{hx} = T_{hx}(y(t))$. The heat transfer from the heat exchangers to the working fluid per unit time is modelled as being governed by the equation:

$$\dot{Q} = T_0 \dot{S} = hA_{hx}[T_{hx}(y(t)) - T_{wf}]. \tag{2}$$

In Eq. (2) as in Ref. [18], T_0 is the equilibrium temperature, $\dot{S}$ the rate of change of entropy flow into/out of the working fluid due to heat transfer, h the (constant) heat-transfer coefficient, A_{hx} the (constant) area over which heat transfer occurs and T_{wf} the temperature of the working fluid at the vapour–liquid interface. The thermal domain must be coupled with the liquid domain by utilising two coupling equations. The entropy flow rate is converted to a volumetric flow rate with:

$$\dot{S} = \rho_g s_{fg} U_{th}, \tag{3}$$

where ρ_g is the density of the vapour and s_{fg} is the specific entropy of vaporisation. The temperatures are converted to pressures with:

$$T_{hx}(y(t)) = \left(\frac{dT}{dP}\right)_{sat} P_{th}; \quad T_{wf} = \left(\frac{dT}{dP}\right)_{sat} P_v, \tag{4}$$

where $(dT/dP)_{sat}$ is the rate of change of working fluid temperature with pressure in the saturation region, P_{th} the thermal pressure and P_v the pressure in the displacer cylinder gas spring. Eqs. (2)–(4) can be combined and rearranged to define a thermal resistance R_{th} and U_{th} as:

$$U_{th} = \frac{P_{th} - P_v}{R_{th}}; \quad R_{th} = \frac{\rho_g s_{fg} T_0}{h A_{hx} (dT/dP)_{sat}}. \tag{5}$$

Eq. (5) is equivalent to Ohm's law for a resistor: $I = \Delta E/R$ [17,18,21,23]. Thus, applying electrical analogies, we can consider entropy change or (volumetric flow rate) to behave like current, and temperature (or pressure) to behave like potential difference.

The heat transfer coefficient h can be estimated by using a correlation from the VDI Heat Atlas [24]:

$$h = h_0 F_{p^*} F_w F_q, \tag{6}$$

where h_0 is a reference heat transfer coefficient for a specific fluid and F are dimensionless functions independent of the fluid. The dependency of h on the pressure in the vicinity of the heat-transfer process is taken into account through F_{p^*}, whilst the material properties of the heat-exchanger wall are accounted for by F_w. Finally, the effect of the heat input Q_{in} (and therefore flux) is considered by F_q. Since h is an input required by the model and Q_{in} is an output of the simulation, h has to be determined iteratively; using Q_{in} from a previous step, h is calculated and the iterations are repeated to convergence.

2.2.2. Fluid domain

The fluid domain comprises the following linear components: displacer cylinder, slide bearing, piston, connection tube, hydraulic accumulators, and hydraulic motor, some of which have already been described by Taleb et al. [25]. Furthermore, it comprises three non-linear components: piston valve and two check valves. The gas spring is modelled both linearly and non-linearly and the two models are compared in Section 3.1.

2.2.2.1. Linear components. In the fluid domain, the viscous drag experienced by the flow (for the liquid phase only) in the connection tube, slide bearing, and displacer cylinder is represented by resistors [22]. The flow is assumed to be quasi-steady, fully developed and laminar, as the Reynolds and Wormersley numbers are sufficiently low. From the simplified Navier–Stokes equation written for the liquid flow in component 'i' one obtains:

$$R_i = \frac{8\mu_l l_i}{\pi r_i^4}, \tag{7}$$

where l_i and r_i are the length and radius of the respective component ('i') and μ_l the dynamic viscosity of the working fluid in the liquid phase. The definitions of the resistances of the components 'i' can be found in Table 1.

To model the resistance of the piston in the slide bearing it is assumed that it is surrounded by a thin lubricating working-fluid film [25]. The resistance of the piston in the slide bearing is:

$$R_{b,p} = \frac{2\mu_l l_{b,p}}{\pi r_p^3 \delta}, \tag{8}$$

where r_p is the radius of the piston and δ the thickness of the lubricating film.

The effect of fluid inertia (as with the resistances, for the liquid phase only) in the connection tube, slide bearing, and displacer cylinder are modelled by inductances [25]. From the simplified Navier–Stokes equation written for the liquid flow in component 'i' one obtains:

$$L_i = \frac{\rho_l l_i}{\pi r_i^2}, \tag{9}$$

where ρ_l is the working-fluid density. The definitions of the respective components 'i' are listed in Table 2. It can be seen that Eq. (9) is equivalent to Faraday's law for an inductor: $\Delta E = L \times dI/dt$ [17].

The hydrostatic pressure in the displacer cylinder, and the compression/expansion processes of the vapour volume at the top of the displacer cylinder and of the volume of gas in the hydraulic accumulators are all modelled by capacitances, which can be described by Gauss' law: $d\Delta E/dt = 1/C \times I$ [17]. From a force balance on the liquid column and if the vapour compression and expansion processes are assumed to be isentropic, one obtains:

$$C_d = \frac{\pi r_d^2}{\rho_l g}; \quad C_i = \frac{V_{0,i}}{\gamma P_0}. \tag{10}$$

In Eq. (10), $V_{0,i}$ and P_0 the equilibrium volume in component 'i' and equilibrium pressure, respectively.

The respective definitions of all capacitances are given in Table 3. A more extensive explanation of the modelling approach for the resistors, inductors and capacitors can be found in Markides and Smith [21], Solanki et al. [17], and Taleb et al. [25].

The piston with the two mechanical springs and surrounding fluid flow is modelled by combining a force balance on the piston

Table 1
Electrical analogy definitions and values for linear components modelled by resistances, see also Refs. [17,23,25]. The unit of all resistances is kg m^{-4} s^{-1}.

Thermal-fluid effect	Component expression	Nominal Value
Connection tube resistance	$R_c = \frac{8\mu_l l_c}{\pi r_c^4}$	4.69×10^3
Hydraulic motor resistance	$R_{hm} = \frac{2\mu_{lub} r_{sh}^3 l_{sh}}{\pi e r_t^4 r_{fm}^2}$	4.31×10^5
Displacer cylinder resistance	$R_d = \frac{8\mu_l l_d}{\pi r_d^4}$	4.25×10^3
Leakage flow resistance 1	$R_{l,1} = \frac{128 c_2 l_p \mu_l}{\pi c_1 c_3}$	5.52×10^7
Leakage flow resistance 2	$R_{l,2} = \frac{128 c_2 l_p \mu_l}{\pi c_1 (c_1 - 2c_2 d_p^2)}$	1.16×10^6
Fluid flow in load pipes ($i = 1, 2$)	$R_{t,i} = \frac{8\mu_l l_{t,i}}{\pi r_{t,i}^4}$	7.44×10^4
Piston resistance	$R_p = \frac{64 l_p \mu_l}{\pi d_p^2 c_1}$	9.20×10^4
Fluid flow resistance in slide bearing	$R_{b,l} = \left(\sum_{i=1}^{n} \frac{\pi r_{ch,i}^4}{8\mu_l l_b}\right)^{-1}$	7.79×10^7
Piston resistance in slide bearing	$R_{b,p} = \frac{2\mu_l l_b}{\pi r_{b,p}^3 \delta}$	1.13×10^6
Thermal resistance	$R_{th} = \frac{\rho_g s_{fg} T_0}{h A_s (dT/dP)_{sat}}$	1.78×10^9

Table 2
Electrical analogy definitions and values for linear components modelled by inductances, see also Refs. [17,23,25]. The unit of all inductances is kg m^{-4}.

Thermal-fluid effect	Component expression	Nominal value
Connection tube inductance	$L_c = \frac{\rho_l l_c}{\pi r_c^2}$	5.07×10^5
Hydraulic motor inductance	$L_{hm} = \frac{8(M_m D_m^2 + M_g D_g^2)}{\pi^2 D_t^4 D_m^2}$	3.09×10^5
Displacer cylinder inductance	$L_d = \frac{\rho_l l_d}{\pi r_d^2}$	1.88×10^5
Leakage flow inductance	$L_l = \frac{64 c_2^2 m_p}{\pi^2 c_1 (c_1 - 2c_2 d_p^2)}$	6.45×10^7
Fluid flow in load pipes ($i = 1, 2$)	$L_{t,i} = \frac{\rho_l l_{t,i}}{\pi r_{t,i}^2}$	2.02×10^6
Piston inductance	$L_p = \frac{32 m_p c_2}{\pi^2 d_p^2 c_1}$	5.96×10^6
Fluid flow inductance in slide bearing	$L_{b,l} = \left(\sum_{i=1}^{n} \frac{\rho_l l_b}{\pi r_{ch}^2}\right)^{-1}$	1.35×10^7
Piston inductance in slide bearing	$L_{b,p} = \frac{\rho_p l_b}{\pi r_{b,p}^2}$	4.42×10^6

Table 3
Electrical analogy definitions and values for linear components modelled by capacitances, see also Refs. [17,23,25]. The unit of all capacitances is $m^4\,s^4\,kg^{-1}$.

Thermal-fluid effect	Component expression	Nominal value
Displacer cylinder capacitance	$C_d = \frac{\pi r_d^2}{\rho_l g}$	9.91×10^{-8}
Leakage flow capacitance	$C_l = \frac{\pi^2 c_1 (c_1 - c_2 d_p^2)}{64 c_2^2 k_{ms}}$	1.78×10^{-10}
Piston capacitance	$C_p = \frac{\pi^2 d_p^2 c_1}{32 k_{ms} c_2}$	6.02×10^{-10}
Linear gas spring displacer cylinder	$C_v = \frac{h_v \pi r_d^2}{P_0 \gamma}$	3.38×10^{-9}
Hydraulic accumulator capacitance ($i = 1, 2$)	$C_{a,i} = \frac{V_{a,i}}{\gamma P_{a,i}}$	3.58×10^{-10}

with the Navier–Stokes equation for the surrounding liquid-flow in the axial direction. Hence, the following equations are used to describe these two components [25]:

$$R_{l,1} = \frac{128 c_2 l_p \mu_l}{\pi c_1 c_3}; \quad R_{l,2} = \frac{128 c_2 l_p \mu_l}{\pi c_1 \left(c_1 - 2 c_2 d_p^2\right)};$$

$$C_l = \frac{\pi^2 c_1 \left(c_1 - c_2 d_p^2\right)}{64 c_2^2 k_{ms}};$$

$$L_l = \frac{64 c_2^2 m_p}{\pi^2 c_1 \left(c_1 - 2 c_2 d_p^2\right)}; \quad R_p = \frac{64 l_p \mu_l}{\pi d_p^2 c_1}; \quad C_p = \frac{\pi^2 d_p^2 c_1}{32 k_{ms} c_2};$$

$$L_p = \frac{32 m_p c_2}{\pi^2 d_p^2 c_1}. \tag{11}$$

In Eq. (11), d_p and m_p are the diameter and mass of the piston respectively, k_{ms} is the spring constant of the upper and lower mechanical springs, and $c_1 = d_c^2 - d_p^2$, $c_2 = \ln(d_c/d_p)$, and $c_3 = c_2\left(d_c^2 + d_p^2\right) - c_1$ are three geometrical constants relating the diameter of the piston and enclosing displacer cylinder.

2.2.2.2. Non-linear components. The piston valve, which is formed between the piston and the displacer cylinder (see Fig. 1), can either be open (when the piston is at or near the top dead centre (TDC) or bottom dead centre (BDC)) or closed (at all other piston positions). When the valve is closed fluid is prevented from flowing from the space above the valve to the slide bearing or vice versa, whilst the piston is still moving. The valve is modelled as a non-linear resistance. The Heaviside step function ($H\{\cdot\}$) is utilised to determine the value of the resistance. It has the form:

$$R_{pv} = R_{min} + \frac{1}{2} R_{max}\left(-H\{P_{l,d} - \rho_l g h_{pv}\} + H\{P_{l,d} + \rho_l g h_{pv}\}\right). \tag{12}$$

In Eq. (12), R_{min} is the flow resistance when the valve is open and R_{max} the resistance when the valve is closed. The value for R_{max} is set much higher than the values of the resistances in its parallel branch (R_p and $R_{b,p}$) to prevent fluid from flowing through the valve when activated by the Heaviside function. $P_{l,d}$ is the hydrostatic pressure difference across the liquid in the displacer cylinder and correlates with the position of the piston, and h_{pv} is a fixed length (by design) that corresponds to the position at which the valve opens/closes.

An additional non-linear resistance is included in the model, which guarantees that the amplitudes of displacement of the piston and liquid column are smaller than the length of the displacer cylinder and hence, the piston and liquid column cannot 'leave' the displacer cylinder. It is defined by the physical dimensions of the displacer cylinder and has the form:

$$R_{nl} = R_{max,nl}\left(H\{P_{l,d} - \rho_l g l_d\} + H\{-P_{l,d} - \rho_l g l_d\}\right), \tag{13}$$

where l_d represents the height of the displacer cylinder, which acts to limit the maximum amplitude of the vertical displacement of the piston.

It is implicit in the non-linear model of the gas spring situated above the piston in the displacer cylinder that the compression and expansion processes of this gas spring are isentropic, and hence governed by $PV^\gamma = \text{const.}$, where P is the pressure in the gas spring and V is the volume of the gas spring. The pressure and the volume can be separated into a mean value (P_0, V_0), when the piston is in the equilibrium position, and a perturbation value (P_v, V_d), so that the total pressure $P = P_0 + P_v$ and total volume $V = V_0 + V_d$ are the sums of mean and perturbation values. The derivative of the volume dV_d/dt is the negative flow rate of working fluid in the gas spring $dV_d/dt = -U_v$. The derivatives of the constant mean pressure and mean volume are by definition zero. Hence, the change of pressure in the gas spring is:

$$\frac{dP_v}{dt} = \frac{\gamma(P_0 + P_v)U_v}{V_0 + V_d}. \tag{14}$$

2.2.2.3. Load components. The flow of the working fluid through the hydraulic motor provides the driving torque for the motor and the coupled power-generating system. This is manifested in the pressure drop across the motor. The forces that present counteracting torques include the inertial force of the motor assembly and the frictional forces between the bearings, shafts, etc. The resultant of these torques gives rise to an angular acceleration of the hydraulic motor. The motor described here is a shaft mounted hydraulic motor; a torque balance on the motor thus results in:

$$(I_{hm} + I_g)\frac{d\omega_{hm}}{dt} = \Delta P A_t \frac{d_{hm}}{2} - F_{fric}\frac{d}{2} - T_{hm}. \tag{15}$$

Here, $A_t = \pi d_t^2/4$ is the cross-sectional area of the working-fluid inlet pipe, d is the diameter of the shaft of length l, T_{hm} is the torque of the power generating system, and ΔP is the pressure drop across the hydraulic motor. With the assumption that the rotating mass of the motor is uniformly distributed about the shaft, $I_{hm} = m_{hm} d_{hm}^2/8$ is the overall rotational inertia of the motor and its couplings with d_{hm} being a representative diameter of the motor. Similarly, the rotational inertia of the generator is $I_g = m_g d_g^2/8$.

The frictional force between the shaft and the motor is defined by applying Newton's law of viscosity to the rotary motion between the motor and its shaft. With a small gap ϵ between the two members and μ_{lub} the dynamic viscosity of the lubricating oil, the frictional force can be simplified to:

$$F_{fric} = \mu_{lub}\pi d l \frac{1}{\epsilon}\frac{\omega_{hm} d}{2}. \tag{16}$$

It is noted that static and Coulomb friction loads will also be present during the operation of the hydraulic motor to a certain degree [26,27]; these are however negligible in comparison to the frictional force [28].

The back torque from the motor and generator assembly T_{hm} is taken as being proportional to its angular velocity [29]. Thus, $T_{hm} = k_{hm}\omega_{hm}$ where k_{hm} is a parameter to be determined for any particular engine set-up. This is done by designing the motor that delivers the maximum power output from the engine. With the assumption that there is no slip between the inlet working-fluid and the rotating parts of the motor, the angular velocity ω_{hm} can be written in terms of the working fluid volumetric flow rate U_{hm} by equating the inlet speed of the working fluid with the tip speed of the motor. Thus:

$$\omega_{hm} = \frac{U_{hm}}{\pi(d_t/2)^2 d_{hm}/2}. \tag{17}$$

Substituting the formulas for I_{hm}, I_g, ω_{hm}, A_t, T_{hm} and F_{fric} in the torque balance in Eq. (15) and simplifying for the pressure drop results in:

$$\Delta P = \frac{8(m_{hm}d_{hm}^2 + m_g d_g^2)}{\pi^2 d_t^4 d_{hm}^2}\frac{dU_{hm}}{dt} + \frac{16\mu_{lub}d^3 l}{\pi\epsilon d_t^4 d_{hm}^2}U_{hm} + \frac{64k_{hm}}{\pi^2 d_t^4 d_{hm}^2}U_{hm}. \quad (18)$$

From Eq. (18) and by comparison with earlier presented electrical analogies in Eqs. (7) and (9), one obtains the expressions for the inductance and resistances associated with the hydraulic motor:

$$L_{hm} = \frac{8(m_{hm}d_{hm}^2 + m_g d_g^2)}{\pi^2 d_t^4 d_{hm}^2}; \quad R_{hm} = \frac{16\mu_{lub}d^3 l}{\pi\epsilon d_t^4 d_{hm}^2}; \quad R_{gen} = \frac{64k_{hm}}{\pi^2 d_t^4 d_{hm}^2}. \quad (19)$$

2.2.3. Up-THERM engine circuit model

The individual components that represent the thermal and fluid domains of the device, which are described in Sections 2.2.1 and 2.2.2, are combined to form an Up-THERM heat-engine network model. This leads to the Up-THERM electrical-circuit representation depicted in Fig. 3. The electrical components in this diagram are interconnected in the same way as they are arranged in the schematic in Fig. 1.

A relationship between the wall temperature of the heat exchanger at the location of the active heat transfer region $T_{hx}(y)$ (Eq. (1)) and the height of the vapour–liquid interface $y(t)$ can be formulated. The wall temperature is converted to the thermal pressure P_{th} (compare Eq. (4)) and the height $y(t)$ is expressed through the hydrostatic pressure difference $P_{l,d} = y\rho_l g$ across the liquid column in the displacer cylinder:

$$P_{th} = \alpha \tanh(\beta P_{l,d}), \quad (20)$$

which is a non-linear static relation for the temperature profile along the heat-exchanger wall.

The model is represented in state-space form. To specify the thermodynamic state of the system, the minimum number of independent thermodynamic variables are required. Kirchhoff's voltage and current laws are employed to formulate one ordinary differential equation (ODE) for each state variable [30]. The state variables are: the hydrostatic pressure in the displacer cylinder, $P_{l,d}$; the time-varying pressure and volume in the displacer cylinder gas spring, P_v and V_d; the pressures over the leakage and piston capacitors $P_{C,l}$ and $P_{C,p}$; the pressures in the hydraulic accumulators $P_{C,a,1}$ and $P_{C,a,2}$; the leakage flow rate $U_{l,2}$; the piston flow rate U_p; the flow rate in the connection tube U; the flow rate in the pipe leading from the hydraulic accumulator to the connection tube $U_{t,1}$; and the flow rate flowing through the hydraulic motor U_{hm}. For numerical reasons, the set of ODEs is non-dimensionalized with the following scaling parameters [18]: the pressure $P^* = 1 \times 10^5$ Pa, the flow rate $U^* = 1 \times 10^{-3}$ m^3 s^{-1}, the volume $V^* = 0.1 \times 10^{-6}$ m^3, and the time $\tau = 1$ s.

The parameters α and β which determine the non-linear temperature profile in the thermal domain are non-dimensionalized to the parameters K and Λ, respectively:

$$K = \frac{\alpha}{P^*(dT/dP)_{sat}}, \quad \Lambda = \frac{\beta P^*}{\rho_l g}. \quad (21)$$

The nominal physical dimensions to calculate the parameters in Tables 2–4 were obtained from drawings made by the company Encontech B.V. [31], who proposed a prototype design of the Up-THERM engine. Water is used as working fluid for the engine, as

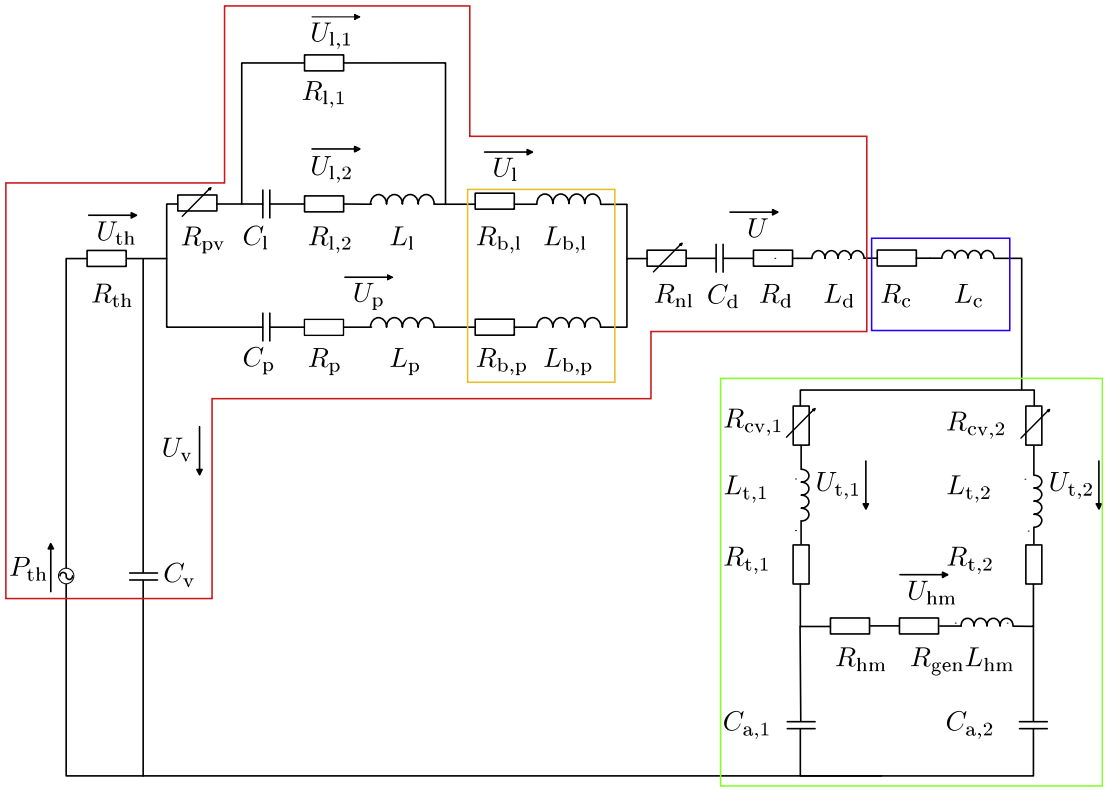

Fig. 3. Circuit diagram of the Up-THERM heat engine; colours correspond to the engine components in Fig. 1. R_i denotes a resistance, L_i an inductance and C_i a capacitance. U_i is the volumetric flow rate through a component. The subscript 'th' denotes the thermal domain. The single components of the fluid domain are the leakage flow denoted by 'l', the piston 'p', the fluid flow in the slide bearing 'b,l', the piston in the slide bearing 'b,p', the connection tube 'c', the liquid column 'd' and the gas spring 'v' in the displacer cylinder, and the non-linear valve formed by the piston and cylinder 'pv'. The load comprises the two check valves 'cv,i', two pipes 't,i', hydraulic accumulators 'a,i' and hydraulic motor 'hm'. (For interpretation of the references to colour in this figure legend, the reader is referred to the web version of this article.)

Table 4
Operating conditions for experiments.

Parameter	Value	Unit
Amplitude	72	mm
Period	40	s
Sample rate	1000	samples/s
T_{cold}	20	°C
T_{hot}	105	°C

it is considered as a working fluid in the prototype engine. Additional working fluids are considered in detail in follow-up paper Ref. [1]. The heat-source temperature is 450 °C since the prototype was operated approximately at this temperature and the heat-sink temperature 10 °C. The equilibrium temperature lays midway between the heat source and sink temperatures, $T_0 = (T_{hot} + T_{cold})/2$.

2.3. Calculation of performance indicators and parametric variations

2.3.1. Solution and parametric study

The Up-THERM model described in the previous sections is solved in MATLAB, which has a number of built-in ODE solvers. The resulting set of ODEs is moderately stiff, and so the solvers ode23t and ode23s are utilised as they have the shortest computation time. Solver ode23t is an implementation of the trapezoidal rule, which is an implicit second-order method, whereas solver ode23s is a one-step solver based on a modified Rosenbrock formula [32].

The model is first solved using the nominal physical dimensions which were provided through drawings from Encontech B.V. [31] at its nominal heat-source temperature of 450 °C. Following this exercise, a parametric study is performed into the effects of variations in the physical dimensions of the Up-THERM engine and changes of the heat-source temperature on the engine's performance, as characterised by three performance indicators: frequency, power output, and exergy efficiency. By changing the physical dimensions, the electrical parameters R, L, and C, which are used in the engine model, vary. Using the heat-source temperature and the heat-sink temperature (which is always held constant at 10 °C) the temperature difference between the heat source and sink can be calculated. This leads to a specific equilibrium temperature, half way between the heat-source and heat-sink temperatures. The fluid properties at this equilibrium temperature are obtained from the NIST database [33]. These properties have also an effect on the R, L, and C parameters used in the model. When the heat-source temperature is changed, α varies, which has an influence on the temperature profile in the heat exchangers. The other parameter β that determines this profile is held constant.

Physical dimensions are varied from a factor of 0.1× to 10× their nominal values whilst all other parameters are held constant. The temperature of the heat source is varied between 400 °C and 500 °C, thereby bracketing the nominal temperature of 450 °C, with the physical dimensions set to their nominal values.

2.3.2. Calculation of performance indicators

After the model has been solved, the amplitudes of all pressures and volumetric flow rates are known. The hydrostatic pressure of the liquid column in the displacer cylinder is used to determine the frequency. Any other pressure or flow rate that oscillates, i.e. that is not in the load arrangement, can be used to determine the frequency. Three consecutive points, at which the pressure amplitudes of $P_{l,d}$ are zero are selected. Between the first and the third point exactly one full cycle occurs. By determining the time between the first and the third point, the frequency can be calculated.

With the flow rate through the hydraulic motor the power output P_{hm} can be calculated as follows:

$$P_{hm} = \int R_{gen} U_{hm} \mathrm{d}V_{load}, \tag{22}$$

where $V_{load} = \int U_{hm} \mathrm{d}t$. For each simulation the value of the useful-power generating resistance R_{gen} is chosen that gives the maximum power output.

Two efficiencies of the Up-THERM engine can be calculated, the thermal and the exergy efficiency (η_{th} and η_{ex}). Due to the low temperature of the heat source, the thermal efficiency is inherently low, so we focus here primarily on the latter. The exergy efficiency is calculated as follows [21]:

$$\eta_{ex} = \frac{P_{hm}}{\int P_{th} \mathrm{d}V_{th}}. \tag{23}$$

In Eq. (23), P_{hm} is the hydraulic power generated at the motor, as given in Eq. (22), P_{th} is the thermal pressure, and V_{th} the thermal volume with $V_{th} = \int (U + U_v) \mathrm{d}t$. Furthermore, the thermal efficiency is:

$$\eta_{th} = \frac{P_{hm}}{\dot{Q}_{in}}, \tag{24}$$

where $\dot{Q}_{in}$ is the rate of heat input over a half cycle defined by $\dot{Q} > 0$ in Eq. (2).

3. Validation of model components

In this section we validate the gas spring model in the displacer cylinder and the temperature profile along the heat-exchanger walls. For the gas spring model we derive a slightly different circuit diagram, which has different values for the electrical components than the ones used in the previous section. When we move on to the Up-THERM model results in the next section we will be using the RLC values from Section 2 again.

3.1. Gas spring model validation methodology

The operation characteristics, in particular the frequency of oscillation, are validated using a similar thermofluidic oscillator, the 'Evaporative Reciprocating-Piston Expander' (ERPE) [25]. For the ERPE, the frequency was determined experimentally for three back pressures (saturation pressure at equilibrium): 9.4, 11.8 and 22 bar. The ERPE consists of the same displacer cylinder as the Up-THERM engine, but instead of a hydraulic motor for power generation and the two accumulators, the ERPE has a further cylinder with a gas spring. The connection tube is split into two branches, both including a check valve to allow flow in only one direction. The check valve in one of the branches comprises an adjustable resistance. A detailed explanation of the model and the experimental methodology can be found in Taleb et al. [25]. The electrical circuit diagram of the ERPE is shown in Fig. 4.

The Up-THERM engine model is amended to reflect the differences in the ERPE. In total three models of the ERPE are compared: (1) one with a linear description of the gas springs, (2) one with a non-linear description of the gas spring in the displacer cylinder and a linear model for the second gas spring, and (3) one with a non-linear description of both gas springs. The linear description of the pressure drop of the second gas spring is:

$$\frac{\mathrm{d}P_{gs}}{\mathrm{d}t} = (\gamma_{ar} P_0)/(V_{0,gs}) U. \tag{25}$$

In Eq. (25), γ_{ar} is the heat capacity ratio of Argon, the medium in the gas spring; P_0 the equilibrium pressure (back pressure); and $V_{0,gs}$ is

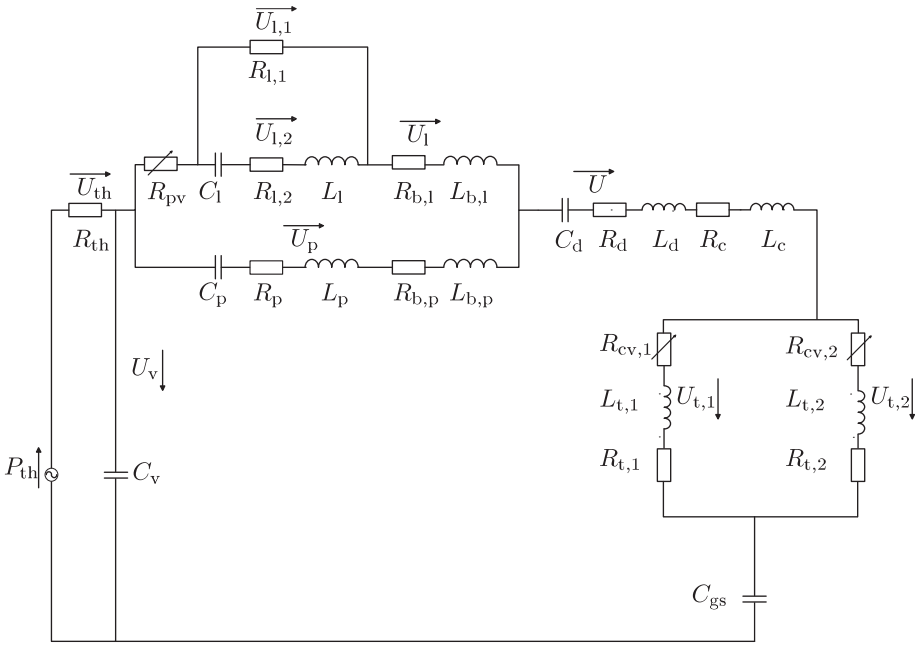

Fig. 4. Circuit diagram of the ERPE. The subscripts are equivalent to those in Fig. 3.

the constant volume of the gas spring in equilibrium. The non-linear description of the pressure drop in this gas spring is:

$$\frac{dP_{gs}}{dt} = \frac{\gamma_{ar}(P_0 + P_{gs})U}{V_{0,gs} + V_{gs}}, \tag{26}$$

with V_{gs} the variable volume in the second gas spring.

3.2. Heat-exchanger temperature profile validation methodology

To obtain a better understanding of the heat transfer process between the heat exchangers of the engine and the phase-changing working fluid, an experimental apparatus was designed to investigate the temperature profile in the heat-exchanger walls. This is the first time that this has been carried out in a thermofluidic oscillator. A schematic of the experimental apparatus is shown in Fig. 5. The set-up comprises an aluminium cylinder with an in-built piston. The piston head is sealed against the cylinder wall and therefore preventing fluid from flowing around the piston head and entering the space below. The piston rod is connected to a pneumatic actuator which imposes a sinusoidal motion on the piston. The period and amplitude of the sine wave can be adjusted to allow for flexible measurement conditions. An electric heater is attached to the top half of the outer wall of the cylinder functioning as the hot heat-exchanger. The temperature of the electric heater can be varied using a PID-controller. Below the heater a plastic tube is coiled around the cylinder. The tube is connected to the water mains, thus functioning as the cold heat exchanger. The space above the piston is initially filled with liquid pentane. During the experiments the pentane evaporates and condenses as it gets in contact with the hot and cold heat exchanger, respectively.

By comparing the experimental set-up in Fig. 5 with the schematic of the engine, Fig. 1, one can observe that the following engine components are represented in the experiments: hot and cold heat exchangers, gas spring in displacer cylinder, and piston. Since only some components of the engine appear in these experiments, the set-up cannot be considered a complete engine prototype.

A pressure transducer is installed to measure the pressure in the vapour space. Additionally, twelve thermocouples (TC1–TC12) are

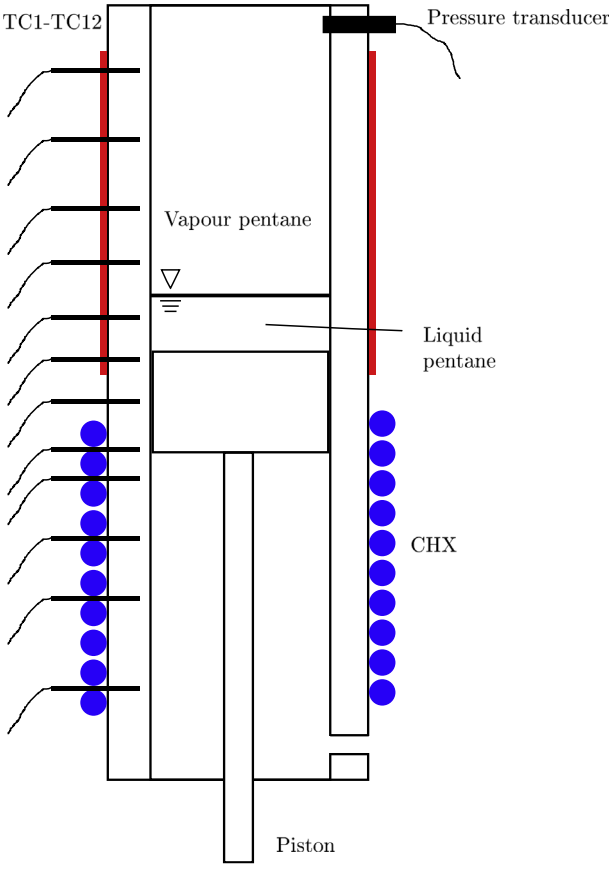

Fig. 5. Schematic of the experimental apparatus with twelve thermocouples (TC1–TC12) and one pressure transducer. At the top half of the cylinder is the hot heat exchanger (HHX) and at the bottom half the cold heat exchanger (CHX).

arranged axially along the cylinder wall to measure the wall temperature. The thermocouples are inserted into the wall with a distance of 1.5 mm from the inner surface. This distance is required to

account for structural feasibility of the cylinder. A micropulse transducer records the position of the piston. The temperatures of the electric heater and the water temperature in the cooling tube are known. With these two temperatures $\alpha = \Delta T_{hx}/2$ can be determined, which is half of the temperature difference between the hot and cold heat exchanger. The second important parameter that defines the temperature profile is β. The product $\alpha\beta$ determines the slope of the temperature profile near the origin, $y = 0$ (see Fig. 2). Parameter β is determined by fitting the measured temperature at each thermocouple to a $\tanh\{\cdot\}$ function. The positions of the thermocouples are known and the fitting function has the form:

$$T_i = \alpha \tanh(\beta y_i), \tag{27}$$

where T_i is the temperature of thermocouple i and y_i its position. To determine the goodness of fit, the coefficient of determination is used [34]. After non-dimensionalizing α and β obtained from this fitting exercise, these parameters can be compared to the values which are used in the model.

The operating conditions of the experiments which are employed to generate the results of the present paper are summarised in Table 4.

3.3. Gas spring model validation results

The frequency of the ERPE was determined experimentally for three back pressures: 9.4 bar, 11.8 bar and 22 bar [25]. The predicted frequencies by three alternative Up-THERM/gas-spring models are compared with the experimentally obtained values in Table 5. The frequency observed in the experiments is ~0.2 Hz for the higher back pressures and 0.02 Hz for the lower one. Given the difficultly of performing some of these experimental tests and the one order of magnitude difference between the results at 9.4 bar and 11.8 bar, it is possible that the lowest back pressure result is unreliable. The Up-THERM model with two non-linear gas springs predicts a frequency of 0.43–0.45 Hz for all back pressures, which is close albeit slightly higher than the experimental values except for the lowest back pressure. The predicted frequency stays almost constant over the investigated back pressure range, also as observed by the intermediate and higher pressure experimental data. The Up-THERM model with only one gas spring described non-linearly predicts a frequency in the range 1.0–1.9 Hz over the range of investigated back pressures. These values are between 10 and 50 times higher than the experimentally observed values. The linear gas spring model predicts a frequency between 3.7 Hz and 6.1 Hz, which is between 30 and 180 times higher than the values observed in the experiments. In the model with no or one gas spring described non-linearly, the frequency rises with increasing back pressure. The model with a non-linear description of both gas springs predicts the frequency in close agreement with the experiments.

Table 5
Comparison of frequencies (Hz) for different pressures.

Gas spring model	Pressure (bar)		
	9.4	11.8	22.0
Linear gas spring	3.70	4.18	6.09
1 Non-linear gas spring	1.00	1.27	1.91
2 Non-linear gas springs	0.45	0.43	0.45
Experiments	0.02	0.20	0.20

3.4. Temperature profile validation results

In Fig. 6 we present the temperature (sampling rate 1000 Hz, averaged over 1 s) plotted against time for each thermocouple. It can be observed that the temperatures of thermocouples TC1–TC10 oscillate around an average temperature whilst the temperatures of thermocouple TC11 and TC12 are approximately constant. The highest oscillations can be observed for thermocouples TC2–TC9, which are in the region in that the piston and the vapour–liquid interface oscillate. These amount to ±2–3 K and are considered small relative to the temperature gradients along the length of the cylinder (~65 K). Due to thermal conduction in the cylinder wall, temperature oscillations can also be observed with thermocouple TC1 and TC10. Thermocouples TC11 and TC12 are too far away from that region.

The equilibrium pressure is 4.15 bar, and the corresponding saturation temperature is 85 °C. The temperature oscillates at all positions apart from TC11 and TC12. For the thermocouples in the hot heat-exchanger region (TC1–TC6), the temperature decreases when the vapour–liquid interface reaches the position of the thermocouple. The evaporation of the working fluid leads to high heat transfer from the hotter wall to the cooler liquid. As the interface moves down, the temperature increases again because the vapour is hotter than the wall. The cooler wall thus receives heat from the hotter vapour and the external heater. What can also be observed at the location of the higher-positioned thermocouples (TC2 and TC3) is that the cooling phase occurs quicker than the heating phase. This is because boiling heat transfer coefficient (cooling phase) is orders of magnitude higher than single phase heat transfer (heating phase). At thermocouple TC1 near the very top of the heat exchanger, the temperature does not oscillate much. The vapour–liquid interface does not reach this height, therefore evaporation does not occur. The small variations in temperature here are due to heat conduction to and from lower parts of the wall.

The thermocouples between the two heat exchangers (TC7) and in the cold heat-exchanger region (TC8–TC12) show the opposite behaviour. The heating phase occurs much quicker than the cooling phase for thermocouples TC7–TC9. Heating occurs when the vapour–liquid interface reaches these positions, and the vapour begins to condense. Due to the high heat transfer coefficient of phase change, a large amount of heat is transferred from the hotter vapour to the cooler wall. When the vapour–liquid interface moves away, heat is transferred from the hotter wall to the cooler bulk liquid and the external cooling water, and the temperature decreases. Because the heat transfer coefficient for single-phase

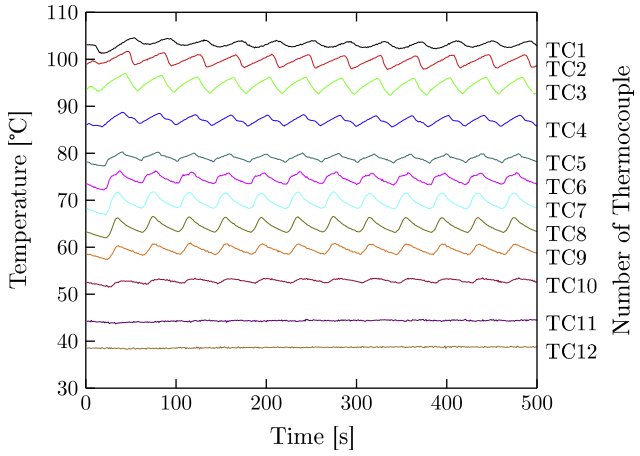

Fig. 6. Temperature of each thermocouple observed during experiments. The numbers on the right-hand side indicate the number of the thermocouple.

heat transfer is low, the temperature decreases more slowly in the cooling phase than it increases in the heating phase. The vapour–liquid interface does not move down to thermocouples TC11 and TC12. Phase change never occurs here, and hence the temperatures are constant.

The time-averaged temperature profile along the cylinder wall is shown in Fig. 7. The black dots correspond to the local temperature of each thermocouple. Using Eq. (27), the measured temperatures, and the positions of the thermocouples, a hyperbolic tangent fit was fitted to the data points, which is represented by the solid line in Fig. 7. The coefficient of determination, which assesses the goodness of the fit [34], is 0.997. Thus, it can be concluded that the $\tanh\{\cdot\}$ function provides a good representation of the temperature profile along the wall, and therefore a $\tanh\{\cdot\}$ function has been used for the heat exchanger temperature profile in the present Up-THERM heat engine model.

In Table 6, we compare the non-dimensional values of K and Λ that are: (a) determined from the experimental data and (b) those used in the Up-THERM model, respectively. Additionally, the product of $K\Lambda$ is given, which determines the slope of the temperature profile at and near the origin ($y = 0$). It can be seen that the value of $K\Lambda$ used in the model is about 10 times larger than that obtained in the experiments, therefore leading to a steeper slope the temperature profile at the origin compared to the experiments. The value used in the Up-THERM model reflects the different solid materials used for the cylinder, with the thermal conductivity of stainless steel (model of Up-THERM device) being about 10 times smaller that of aluminium (experimental validation testing), which would act to sustain the greater temperature gradients in the solid, in agreement with the above observations.

Table 6
Comparison of the non-dimensional parameters, which determine the temperature profile.

Experiments			Model		
K	Λ	$K\Lambda$	K	Λ	$K\Lambda$
4.53	108	490	44.1	101	4440

4. Results and discussion

4.1. Nominal operation

At first the Up-THERM engine model is solved for a nominal configuration, with the values for the R, L, and C parameters taken from Tables 2–4. The power output, efficiencies and frequency for the nominal configuration of the engine can be found in Table 7. All performance indicators vary when the physical dimensions (lengths, diameters) or the working fluid properties change. The working fluid properties are influenced by the heat-source temperature and the choice of working fluid. In the next section we investigate the influence of the physical dimensions and the heat-source temperature on the engine's performance.

From Figs. 8 and 9 it can be observed that a limit cycle can be achieved after about twelve seconds. For longer times the oscillations are sustained and have equal amplitudes.

In Fig. 8, the volumetric flow rate is plotted over time for three components of the engine. Those are the flow rate through the connection tube U, the hydraulic motor U_{hm}, and the tube between the check valve and hydraulic accumulator before the hydraulic accumulator $U_{\mathrm{t,1}}$. The flow rate U_{hm} is always positive and has small

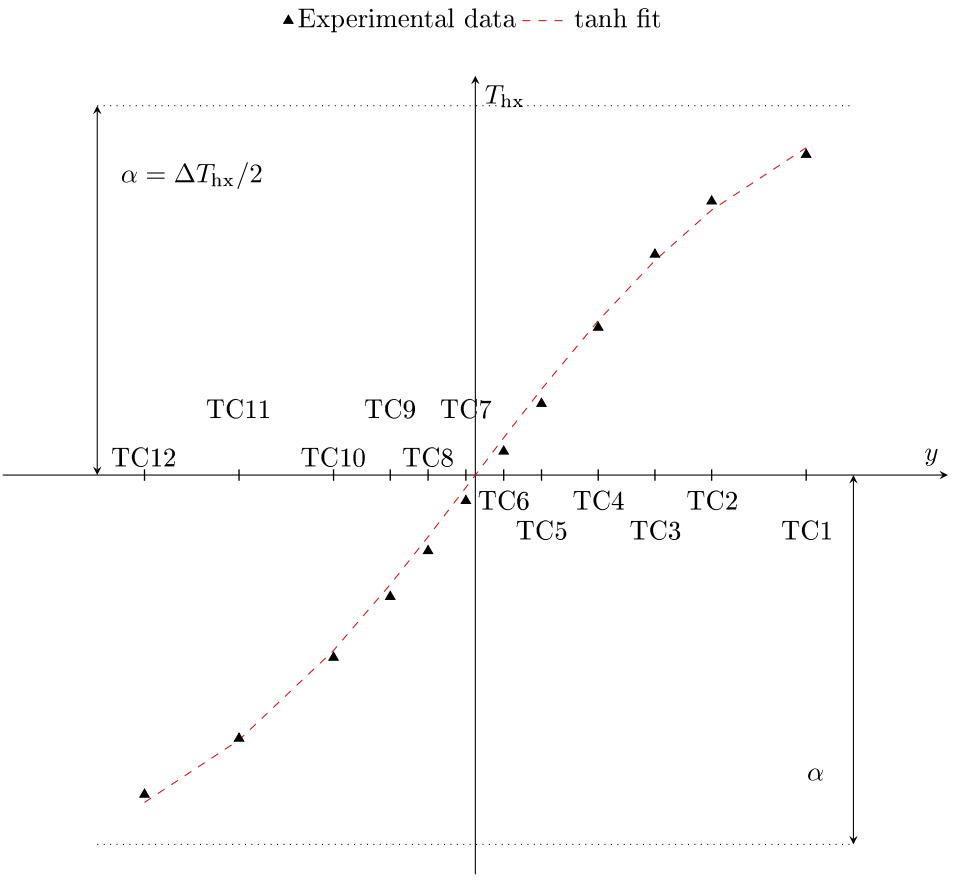

Fig. 7. Temperature profile of the cylinder wall observed during experiments. The black dots represent the temperature measurement at each thermocouple (TC1–TC12) and the solid line the fitted tanh function from the measurement data. The coefficient of determination for the fit is 0.997.

Table 7
Model results for the nominal operation of the Up-THERM heat engine.

Power output	25 W
Exergy efficiency	0.77%
Thermal efficiency	0.2%
Frequency	2.8 Hz

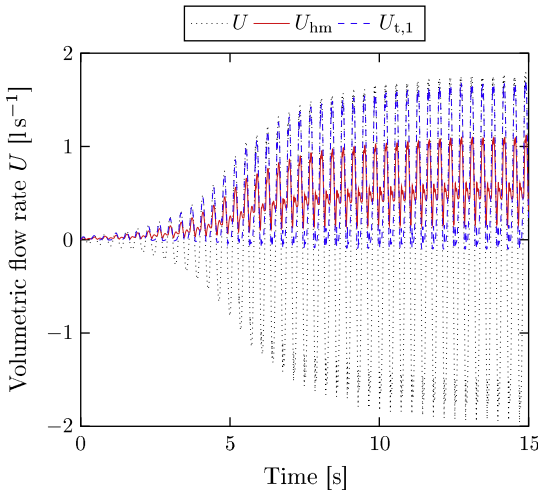

Fig. 8. Volumetric flow rate against time in three components.

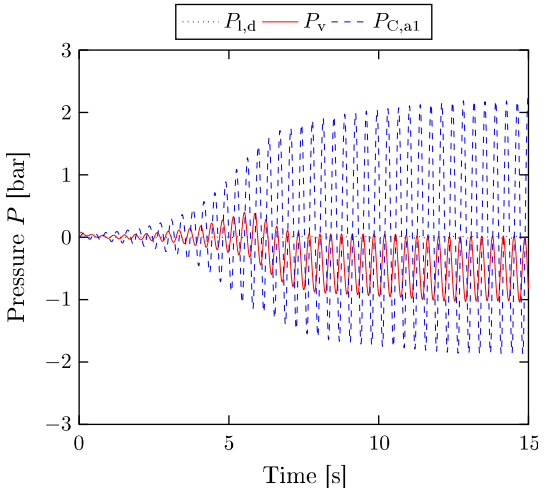

Fig. 9. Pressure against time in various components.

amplitudes compared to U and $U_{t,1}$. U_{hm} is always positive because of the two check valves, and the oscillations are damped by the two hydraulic accumulators.

The check valves prevent $U_{t,1}$ from having large negative amplitudes. (Only a small amount of liquid flows back before the valve closes.) When the valve is fully open, the flow rates $U_{t,1}$ and U are identical. This means that all the liquid from the connection tube flows through the check valve into the hydraulic motor. Finally, the flow rate in the connection tube U oscillates around zero with equal negative and positive amplitudes, as there are no flow restrictions.

In Fig. 9, the temporal variations of pressures in three components are shown. $P_{l,d}$ is the hydrostatic pressure of the liquid in the displacer cylinder below the piston, and thus represents the variation of the height of the liquid column below the piston. It can be seen that its amplitude is low compared to P_v, which is the pressure in the displacer cylinder gas spring, and $P_{C,a1}$, the pressure in the hydraulic accumulator. The maximum amplitude of the liquid column is restricted by the size of the engine, in particular the length of the heat exchanger. Thus, a maximum pressure amplitude of 0.015 bar can be achieved for the hydrostatic pressure, which corresponds to a heat exchanger length of 0.17 m.

The mean pressure in the displacer cylinder gas spring P_v becomes negative for times larger than 5 s. At the same time the mean volume in the displacer cylinder gas spring V_d, Fig. 10, becomes positive. This means that the initially chosen volume of the displacer cylinder gas spring was too small and that for continuous operation of the engine a larger volume is required. The pressure and volume are related through $PV^{\gamma} = \text{const.}$, so that an increase in volume relates to a decrease in pressure.

The pressure in the hydraulic accumulator has the largest amplitudes of the pressures shown. The pressure oscillations are due to liquid flowing in and out of the hydraulic accumulator ($U_{t,1}$), whilst the fluctuations of pressure in the displacer cylinder gas spring are due to the working fluid evaporating and condensing periodically (U_v). The size of the flow rate amplitudes $U_{t,1}$ are equal to the amplitudes of U, see Fig. 8. The flow rate U is the sum of the flow rates U_v and U_{th}, see Fig. 3, with $U_v \ll U_{th}$. Although the volume of the displacer cylinder gas spring is much smaller than the volume of the hydraulic accumulator, and hence its capacitance, the pressure amplitudes in the hydraulic accumulator are bigger than in the displacer cylinder gas spring.

In Fig. 11a is the volume V_{th} plotted over time. It is the volume generated due to the exergy input with $V_{th} = \int U_{th} dt$. It corresponds to the entropy input into the engine. The entropy is linked to the volume trough Eq. (3).

In Fig. 11b is the thermal pressure plotted over time. The pressure is generated due to the exergy input. It corresponds to a temperature and the pressure is coupled with the temperature through Eq. (4). Using the thermal volume V_{th} and the thermal pressure P_{th} one can calculate the exergy input into the engine with: $E = \int P_{th} dV_{th}$.

4.2. Parametric study

The results of the parametric study are shown in Figs. 12–14, where the superscript '$*$' is used to denote the physical dimensions normalised by their respective nominal values. It should be noted that a limit cycle could not be achieved for a value of the displacer cylinder diameter d_d above 1.6× of its nominal value, a connection tube diameter d_c of 0.1× its nominal value, and a gas-spring height

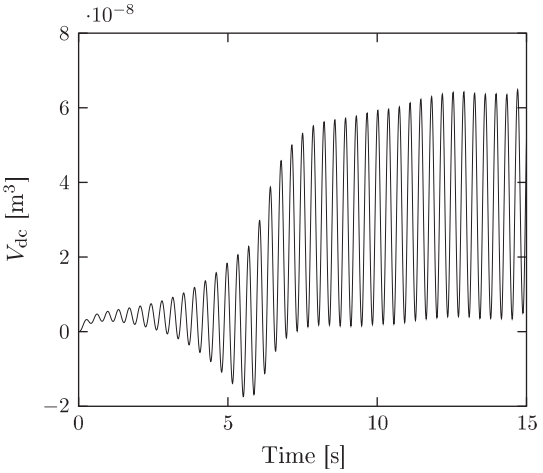

Fig. 10. Volume oscillations in the displacer cylinder gas spring over time.

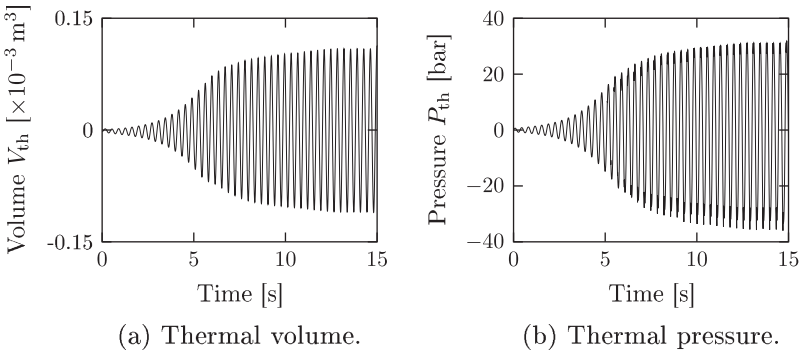

(a) Thermal volume. (b) Thermal pressure.

Fig. 11. Volume and pressure in the thermal domain plotted against time.

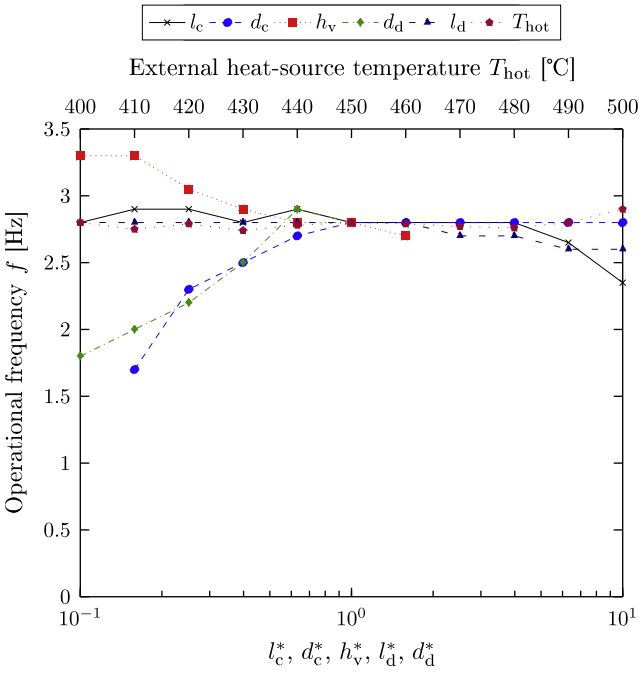

Fig. 12. Influence of physical dimensions and heat-source temperature on the operational frequency. T_{cold} is constant at 10 °C.

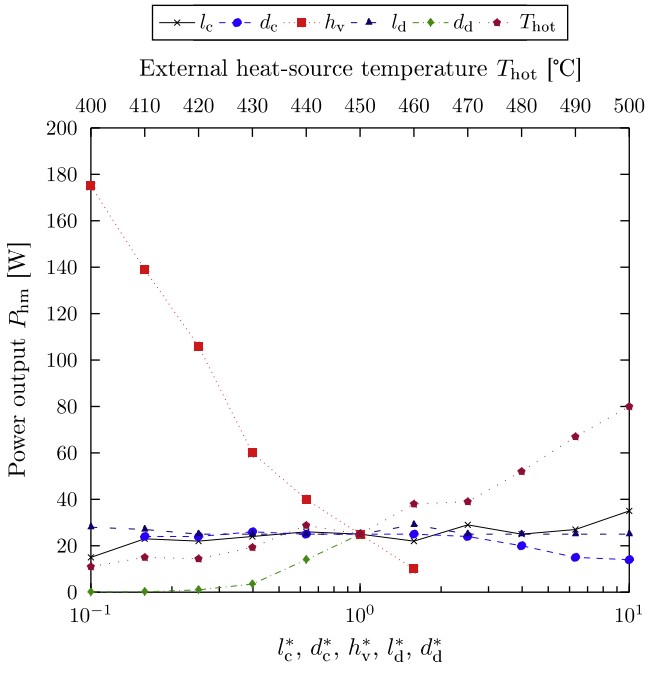

Fig. 13. Influence of physical dimensions and heat-source temperature on power output. T_{cold} is constant at 10 °C.

larger than 2.5× of its nominal value. For the displacer cylinder diameter and the gas-spring height this is due to the increasing equilibrium volume of the gas spring, which makes it softer and hence, the force exerted by the spring is too weak to sustain oscillations. A connection tube that is too thin imposes too great a resistance to the volumetric displacement and hence the oscillations are damped.

In Fig. 12, the operational (oscillation) frequency of the UpTHERM is plotted against varying physical dimensions and heat source temperatures. It can be observed that the length of the connection tube l_c, the length of the displacer cylinder l_d, and the heat-source temperature T_{hot} have almost no influence on the frequency. A slight decrease in the frequency can be observed only for long-length components, i.e. connection tubes and displacer cylinders both longer than 4× their respective nominal lengths. From Tables 1 and 2 it can be seen that the inductances L_c and L_d and the resistances R_c and R_d of the connection tube and displacer cylinder, respectively, are at least one order of magnitude smaller than all other inductances and resistances in the circuit. Increasing the lengths of the connection tube and displacer cylinder by the above mentioned factors (or more), gives rise to values of the corresponding inductances and resistances in the same order of magnitude as the other inductances and resistances in the circuit, at which point these components start to have an influence on the engine's performance.

The fluid properties (except in the thermal resistance) vary by a maximum of 20% when the heat source temperature varies between 400 °C and 500 °C. Thus, as the fluid properties influence the resistances and inductances linearly, those dimensions do not vary by more than 20%.

By increasing the height of the gas spring h_v the frequency decreases. The maximum value of the frequency (3.3 Hz) can be observed for gas-spring heights of 0.1× the nominal value. Increasing the height of the gas spring results in greater values of C_v (compare Table 3) and the gas spring becomes 'softer'. Low values of h_v result in a 'harder' gas spring, which leads to an increased frequency.

Furthermore, increasing the diameters of the connection tube d_c or of the displacer cylinder d_d when these parameters have values lower than their nominal values gives rise to an increasing frequency. For values of d_d^* and d_c^* greater than their nominal values the frequency remains constant. The connection tube and displacer

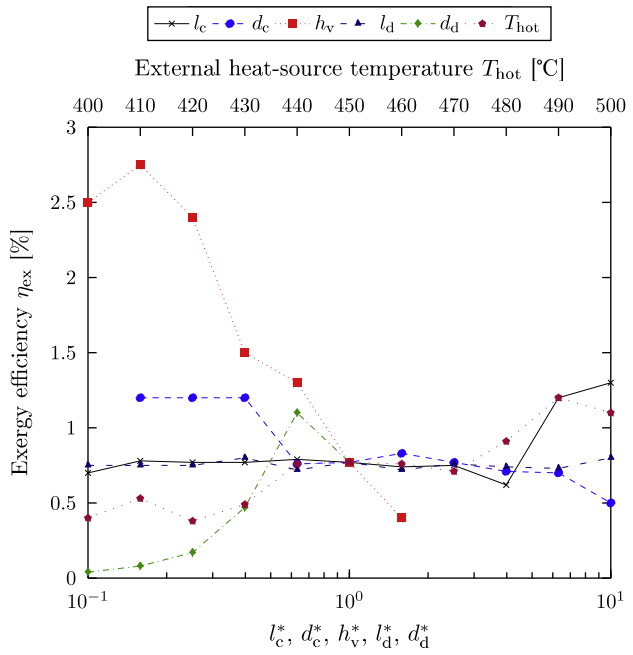

Fig. 14. Influence of physical dimensions and heat-source temperature on exergy efficiency. T_{cold} is constant at 10 °C.

cylinder diameters have an influence on the resistances, inductances and capacitances of the respective liquid columns. Decreasing the diameter increases the resistance and inductance and decreases the capacitance, see Tables 2–4. As the inductances and resistances are proportional to the inverse square of the diameter, the inductances and resistances become disproportionately large for small changes in the values of d_d and d_c, especially when these are small. As the diameters become larger than the nominal values, the values of the inductances and resistances become much smaller than the other inductances and resistances in the cycle and hence, their influence becomes negligible.

Collectively, the results show that h_v, d_d, and d_c have the biggest influence on the frequency of the Up-THERM device. These three dimensions determine the size of the gas spring in the displacer cylinder and hence its hardness, and the width of the liquid columns in the displacer cylinder and connection tube. A softer gas spring results in a decreasing frequency. A thinner liquid column leads also to a lower frequency.

In Fig. 13 the power output is plotted against varying values for the normalised physical dimensions and the heat-source temperature. The length of the displacer cylinder l_d, the length of the connection tube l_c and its diameter d_c have almost no influence on the power output compared to the other dimensions. Comparing with Table 1 it can be seen that the values of the connection tube and displacer cylinder resistances are at least one order of magnitude lower than the resistances of the other components. Since resistances are the only component where power can be dissipated, any power that is dissipated in these components is not used in the hydraulic motor to produce useful work (power).

A smaller height of the gas spring h_v results in a higher power output, which is the product of the volumetric displacement of the liquid and the frequency. By comparing with Fig. 12, one can see that the frequency increases for a shorter height of the gas spring, thereby also increasing the power output.

Increasing the diameter d_d of the displacer cylinder results in an increasing power output. A small diameter of the displacer cylinder results in a high resistance in this component, leading to more power being dissipated and hence less available power in the hydraulic motor that can be converted into useful work. By increasing the diameter of the displacer cylinder d_d, the heat exchanger area increases, which in turn leads to more heat input into the cycle. In addition the volume of the displaced liquid increases, which results in more liquid that can be evaporated/condensed, subsequently driving oscillations of flow and pressure through the hydraulic motor. These two effects lead to an increased power output.

An increasing temperature of the heat source, and thereby increasing the temperature difference between the heat source and heat sink, leads to an increased power output. More heat can be added to the cycle, which in turn can be converted to useful work. Furthermore, with increasing heat-source temperature the heat transfer coefficient increases, which leads to a reduced thermal resistance and increased power output.

In a recently tested prototype of the (nominal design) engine a power output of 20 W was measured [35]. The engine operated with water as working fluid and an electrical heater set to a temperature of 600 °C. However, it was reported that the temperature of the heat-exchanger wall, which is the temperature that is regarded as the heat-source temperature in this paper, was approximately 100–150 °C lower than the temperature of the electrical heater, due to heat losses. From Fig. 13 it can be seen that the present simulations predict a power of 25 W for the corresponding nominal design and heat-source temperature, which is slightly higher than the reported 20 W; this is however considered very good agreement given the nature of the simple modelling approach taken in the present work, the uncertainty in some important geometrical dimensions (e.g. the gas-spring heights could not be measured in the prototype testing), as well as experimental errors.

In Fig. 14, the exergy efficiency is plotted against the varying physical dimensions and heat-source temperatures. The length l_c and diameter d_c of the connection tube and the length of the displacer cylinder l_d have a small influence on the efficiency. These three parameters change the connection tube resistance R_c and the displacer cylinder resistance R_d. Since these resistances are several orders of magnitude smaller than the other resistances, varying them does not considerably change the engine's performance.

Increasing the diameter of the displacer cylinder d_d leads to a sharp increase of the efficiency. A larger diameter of the displacer cylinder leads to a higher volumetric flow rate that is supplied to the hydraulic load and reduced frictional losses in the displacer cylinder, as R_d is decreasing (compare Table 1). Increasing the height of the gas spring h_v leads to a decrease of the efficiency. As with the diameter of the displacer cylinder d_d, making the gas spring smaller (or displacer cylinder wider), the power output and efficiency increase. This means that the additional exergy supplied to the cycle is transformed into useful power in the load.

The temperature of the heat source has a beneficial influence on the efficiency when increased. When the temperature difference between the heat source and heat sink increases, the oscillations of pressure and volumetric displacement increase in magnitude. This results in an increase in the flow rate through the hydraulic motor U_{hm}, which in turn increases the power output from the motor for which: $P_{hm} = \int P_{load} dV_{load}$, with $P_{load} = R_{gen} U_{hm}$ and $V_{load} = \int U_{hm} dt$.

In summary, the following parameters have significant influence on the performance indicators; the heat-source temperature T_{hot}, the displacer cylinder diameter d_c, and the gas spring height h_v. An efficient, high-power, and high-frequency engine will have a small gas-spring height and a medium to large displacer cylinder diameter. A higher heat-source temperature leads to a high efficiency and high power output.

Obtaining a better understanding of the exergy destruction in the engine is essential for an optimised early-stage design. To this

end, we quantify the exergy that is made available to the load arrangement. This is also the exergy of the working fluid at the end of the connection tube which is henceforth called device exergy: $E_{\text{device}} = \int P_c dV_c$, where P_c is the pressure oscillations in the connection tube and V_c its volume oscillations with $V_c = \int U dt$. With the exergy input and the device exergy a device exergy efficiency can be calculated: $\eta_{\text{ex,device}} = \int P_c dV_c / \int P_{th} dV_{th}$.

Fig. 15 shows two pairs of pressure–volume diagrams for two different engine configurations: (a) the nominal configuration; and (b) a high exergy-efficiency and high power-output device configuration. Each pair consists of the pressure and volume that occur in the thermal domain (black solid line, P_{th}–V_{th}) and in the connection tube (red dotted line, P_c–V_c), respectively. The area inside the P_{th}–V_{th} cycle of the thermal domain represents the exergy input to the engine whilst the area inside the P_c–V_c cycle of the connection tube represents the exergy that is available at the load arrangement (end of the connection tube). Due to losses in the displacer cylinder and connection tube, this area is smaller than the area of the exergy input.

The plots are equivalent to *T*–*S* diagrams, since a temperature can be converted into a pressure *P* and the entropy can be converted into a volume *V*. For a detailed description of the coupling equations between pressure and temperature, and entropy and volume, see Section 2.2.1.

Fig. 15a shows *P*–*V* cycles for the nominal operation of the Up-THERM engine. The exergy input into the cycle is 1.3 kJ, and the device exergy is 25 J. This corresponds to a device exergy efficiency of 2%. This efficiency is about 3× higher than the overall exergy efficiency of the engine, including the load arrangement, as reported in Table 7. This implies that for the nominal design most of the exergy input is dissipated in the displacer cylinder, or before the flow has been rectified, however about 2/3 of the available exergy of the device are destroyed in the load arrangement.

The *P*–*V* cycles shown in Fig. 15b are for a high exergy-efficiency and high power-output case. In this case, the exergy input to the cycle is 2.9 kJ and the exergy that is available at the end of the connection tube is 740 J. This corresponds to a device exergy efficiency of 25%. The area enclosed by the *P*–*V* cycle depends on the amplitude of the pressure and volume. The enclosed area here is larger than that for the nominal case, hence, a higher power output is available from this engine configuration. The two peaks that are indicated on the two plots are due to the solid piston hitting the top and bottom of the displacer cylinder. This causes the piston to decelerate suddenly, which rapidly increases the pressure due to inertia.

Comparing Fig. 15a and b one can see that in the cycle configuration shown in Fig. 15a most of the exergy is destroyed in the device, which results in the lower device exergy efficiency. As the device exergy is the maximum available exergy that can be transformed into useful work, this configuration of displacer cylinder and connection tube is not favourable. In Fig. 15b the device exergy efficiency is much higher, which makes this design of the displacer cylinder and connection tube favourable.

4.3. Comparison to the NIFTE and further discussion

In this section a comparison is made between the Up-THERM engine and the NIFTE device as presented in Markides et al. [18]. Both two-phase thermofluidic oscillators have in common an externally imposed constant temperature difference between the hot and cold heat exchangers. This temperature difference together with the reciprocating flow of the working fluid within the device give rise to alternating phase change (evaporation and condensation) of the working fluid leading to periodic oscillations of pressure and volumetric displacement. The temperature profile over the heat-exchanger walls can in both cases be modelled as a tanh{·} function. However, there are also significant differences in the designs of the two engines. Whilst the Up-THERM engine comprises only a displacer cylinder with a moving solid piston, the NIFTE has a displacer and a power cylinder but lacks the solid piston. Furthermore, whereas the Up-THERM is used in conjunction with a hydraulic motor to convert the fluid oscillations into shaft work, the NIFTE has been primarily envisioned as a fluid pumping device [36]. Nevertheless, as stated earlier, although the specifics of the designs of the two thermofluidic oscillators differ to some extent, these devices belong to the same class of systems and their basic principles of operation are similar. It is therefore of interest to compare the two systems more carefully.

The frequencies of operation of the NIFTE and Up-THERM heat engines do not depend on the temperature difference imposed on these devices by the heat source and sink. However, the load flow rate in the NIFTE increases when the temperature difference increases. This flow rate is the useful volumetric flow rate of fluid that can be pumped by the NIFTE pumping device. In the Up-THERM engine this can be compared to the power output, which is dependent on the volumetric flow rate through the hydraulic motor. The power output increases with increasing temperature difference between heat source and heat sink. Thus, the power output of both engines can be increased independently of the frequency by increasing the temperature difference.

On the other hand, while it was reported that the exergy efficiency of the NIFTE does not depend on the temperature difference imposed on the device, it has been observed here that the temperature difference does influence the exergy efficiency of the

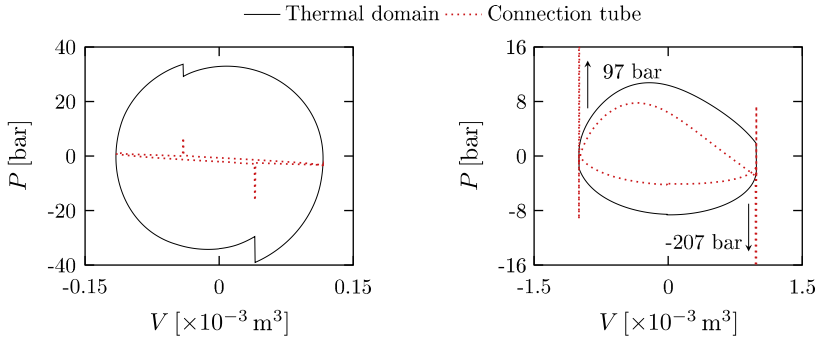

(a) Nominal operating conditions. (b) High power output.

Fig. 15. Pressure volume plots in the thermal domain and connection tube for one full cycle. The area enclosed by the black solid line represents the exergy input and the area enclosed by the red dotted line the exergy that is available at the connection tube. (For interpretation of the references to colour in this figure legend, the reader is referred to the web version of this article.)

Up-THERM engine. Finally, a higher-frequency-content 'beating' behaviour was observed experimentally in the NIFTE, which was captured by the non-linear model in Ref. [18]. Although more complex and broadband, the Up-THERM model also shows higher-frequency 'jumps' in the thermal pressure and pressure in the connection tube, see Fig. 15a and b. Thus, in both cases it can be said that the non-linear descriptions of these engines allow for more realistic predictions of actual engine operation and performance.

5. Conclusions

A non-linear modelling framework has been proposed for a novel two-phase thermofluidic oscillator (heat-engine) concept, termed Up-THERM, which relies on the periodic phase change of a working fluid and the resulting vertical reciprocating motion of a single solid piston within the device. The advantage of the Up-THERM engine concept arises from its small number of moving parts, which results in low capital and maintenance costs. This is particularly useful in low-power applications in remote areas or developing countries, where low up-front costs are crucial.

Alternating phase change (evaporation and condensation) of the working fluid within the Up-THERM device results in periodic oscillations of pressure and flow rate, which can be transformed into a unidirectional flow of working fluid through a hydraulic motor circuit in order to extract power. Important components, such as a gas spring in the device's displacer cylinder, check valves and a piston valve formed between the solid piston and walls of the displacer cylinder, and the temperature profile along the heat exchanger surfaces of the engine were modelled non-linearly. A comparison between the linear and non-linear exchanger surfaces of the gas spring was performed and the frequency predictions of these models were validated against experimental data from a similar engine. The model was amended to describe the engine which was used in these experiments. The non-linear gas spring model described the frequency more realistically compared to its linear counterpart. In addition, an experimental apparatus was constructed and measurements were performed to validate the temperature profile along the heat-exchanger surfaces. A $\tanh\{\cdot\}$ profile was used in the model corresponding to the temperature profile observed in these experiments.

A nominal Up-THERM engine configuration was investigated with respect to three performance indicators: oscillation frequency, power output and exergy efficiency. Following this, a parametric study was performed to investigate the influence of key engine dimensions on the same indicators. It was observed that the dimensions of the displacer cylinder (including the gas spring at the top of the cylinder) and the heat-source temperature have the biggest influence on the power output and efficiency of the engine. For a higher power output, efficiency and frequency, the height of the displacer cylinder gas spring should be shorter than the nominal value, whilst the diameter of the displacer cylinder should be near the nominal value or slightly larger.

A maximum exergy efficiency of 2.8% and a maximum power output of 175 W were observed at the proposed operating temperature of 450 °C for a nominal Up-THERM design (based an the physical dimensions of a device prototype and water as the working fluid), but with shorter displacer cylinder gas-spring height relative to the nominal design. Increasing the diameter of the displacer cylinder increased the exergy efficiency gradually. Exergy efficiency values of 1.2% and power outputs of 80 W were demonstrated at highest investigated heat-source temperatures of 490–500 °C with the nominal design. The present model predicts a power output of 25 W at the nominal design and heat-source temperature; corresponding prototype tests reported an output of 20 W.

Acknowledgements

This work was supported by the UK Engineering and Physical Sciences Research Council (EPSRC) [grant number EP/J006041/1]. The research leading to these results has also received funding from the European Community's Seventh Framework Programme (FP7/2007–2013) under grant agreement number [605826]. O.A. Oyewunmi gratefully acknowledges the funding awarded to him by the Nigerian government which allowed him to embark on this research. Data supporting this publication can be obtained on request from cep-lab@imperial.ac.uk.

References

[1] Oyewunmi OA, Kirmse CJW, Haslam AJ, Müller EA, Markides CN. Working-fluid selection and performance investigation of a two-phase single-reciprocating-piston heat -conversion engine. Appl Energy 2017;186:376–95.
[2] Bhattacharyya SC. Fossil-fuel dependence and vulnerability of electricity generation: Case of selected European countries. Energy Policy 2009;37(6):2411–20.
[3] Hettiarachchi HDM, Golubovic M, Worek WM, Ikegami Y. Optimum design criteria for an organic Rankine cycle using low-temperature geothermal heat sources. Energy 2007;32(9):1698–706.
[4] Zhang HL, Baeyens J, Degrève J, Cacères G. Concentrated solar power plants: Review and design methodology. Renew Sustain Energy Rev 2013;22:466–81.
[5] Markides CN. The role of pumped and waste heat technologies in a high-efficiency sustainable energy future for the UK. Appl Therm Eng 2013;53(2):197–209.
[6] Markides, C. N. Low-concentration solar-power systems based on organic Rankine cycles for distributed-scale applications: Overview and further developments. Front Energy Res 2015;3(47):1–16.
[7] Feldman KTJ. Review of the literature on Sondhauss thermoacoustic phenomena. J Sound Vib 1968;7(1):71–82.
[8] Sondhauss C. Über die Schallschwingungen der Luft in erhitzten Glasröhren und in gedeckten Pfeifen von ungleicher Weite. Ann Phys 1850;155(1):1–34.
[9] Wheatley J, Hofler T, Swift G, Migliori A. An intrinsically irreversible thermoacoustic heat engine. J Acoust Soc Am 1983;74(1):153–70.
[10] Wheatley J, Hofler T, Swift GW, Migliori A. Experiments with an intrinsically irreversible acoustic heat engine. Phys Rev Lett 1983;50(7):499–502.
[11] Ceperley PH. A pistonless Stirling engine-the traveling wave heat engine. J Acoust Soc Am 1979;66(5):1508–13.
[12] Backhaus S, Swift GW. A thermoacoustic-Stirling heat engine: Detailed study. J Acoust Soc Am 2000;107(6):3148–66.
[13] Stammers CW. The operation of the Fluidyne heat engine at low differential temperatures. J Sound Vib 1979;63(4):507–16.
[14] Smith TCB. Asymmetric heat transfer in vapour cycle liquid-piston engines. In: Proceedings of the 12th international stirling engine conference technology exhibition. p. 302–14.
[15] Smith TCB. Thermally driven oscillations in dynamic applications, Ph.D. thesis. University of Cambridge, Cambridge, UK; 2006.
[16] Smith TCB. Power dense thermofluidic oscillators for high load applications. In: Proceedings of the 2nd international energy conversion on engineering conference, Providence (RI). p. 1–15.
[17] Solanki R, Mathie R, Galindo A, Markides CN. Modelling of a two-phase thermofluidic oscillator for low-grade heat utilisation: Accounting for irreversible thermal losses. Appl Energy 2013;106:337–54.
[18] Markides CN, Osuolale A, Solanki R, Stan G-BV. Nonlinear heat transfer processes in a two-phase thermofluidic oscillator. Appl Energy 2013;104:958–77.
[19] Glushenkov M, Sprenkeler M, Kronberg A, Kirillov V. Single-piston alternative to Stirling engines. Appl Energy 2012;97:743–8.
[20] Huang BJ, Chuang MD. System design of orifice pulse-tube refrigerator using linear flow network analysis. Cryog 1996;36(11):889–902.
[21] Markides CN, Smith TCB. A dynamic model for the efficiency optimization of an oscillatory low grade heat engine. Energy 2011;36(12):6967–80.
[22] Solanki R, Galindo A, Markides CN. Dynamic modelling of a two-phase thermofluidic oscillator for efficient low grade heat utilization: Effect of fluid inertia. Appl Energy 2012;89(1):156–63.
[23] Solanki R, Galindo A, Markides CN. The role of heat exchange on the behaviour of an oscillatory two-phase low-grade heat engine. Appl Therm Eng 2013;53(2):177–87.
[24] VDI Gesellschaft. VDI Heat Atlas. Springer; 2010.
[25] Taleb AI, Timmer M, Elshazly MY, Samoilov A, Kirikkov VA, Markides CN. A single-reciprocating-piston two-phase thermofluidic prime-mover. Energy 2016;140:250–65.
[26] Hibi A, Ichikawa T. Mathematical model of the torque characteristics for hydraulic motors. Bull Jpn Soc Mech Eng 1977;20(143):616–21.
[27] McCandlish D, Dorey RE. The mathematical modelling of hydrostatic pumps and motors. Proc Inst Mech Eng, Part B: J Eng Manuf 1984;198(3):165–74.
[28] Merit HE, Gavin JT. Friction load on hydraulic servos. Proceedings of the national conference on industrial hydraulics, vol. 16. p. 174–84.
[29] Merritt HE. Hydraulic control systems. John Wiley & Sons; 1967.

[30] Martinez-Marin T. State-space formulation for circuit analysis. IEEE Trans Edu 2010;53(3):497–503.
[31] Encontech BV. Up-THERM: Innovative high efficiency phase change fluid based heat engine. http://www.encontech.nl/papers/UpTHERM-Flyer.pdf [accessed 5 April, 2016].
[32] Shampine L, Reichelt M. The MATLAB ODE suite. SIAM J Sci Comput 1997;18 (1):1–22.
[33] Lemmon EW, Huber ML, McLinden MO. NIST standard reference database 23: Reference fluid thermodynamic and transport properties – REFPROP. National Institute of Standards and Technology, Standard Reference Data Program 9.1.
[34] Ross SM. Introduction to probability and statistics for engineers and scientists. 4th ed. University of Southern California, Los Angeles, USA: Academic Press; 2009.
[35] Glushenkov M, Sprenkeler M, Kronberg AE. Regenerative heat to mechanical energy converter with dense working fluid. Personal communication; 2014.
[36] Markides CN, Gupta A. Experimental investigation of a thermally powered central heating circulator: Pumping characteristics. Appl Energy 2013;110: 132–46.